

# Journal of Materials Chemistry A

Accepted Manuscript



This is an *Accepted Manuscript*, which has been through the Royal Society of Chemistry peer review process and has been accepted for publication.

*Accepted Manuscripts* are published online shortly after acceptance, before technical editing, formatting and proof reading. Using this free service, authors can make their results available to the community, in citable form, before we publish the edited article. We will replace this *Accepted Manuscript* with the edited and formatted *Advance Article* as soon as it is available.

You can find more information about *Accepted Manuscripts* in the [Information for Authors](#).

Please note that technical editing may introduce minor changes to the text and/or graphics, which may alter content. The journal's standard [Terms & Conditions](#) and the [Ethical guidelines](#) still apply. In no event shall the Royal Society of Chemistry be held responsible for any errors or omissions in this *Accepted Manuscript* or any consequences arising from the use of any information it contains.



## Cu-BTC MOF / Graphene-based hybrid materials as low concentration ammonia sensors

Nikolina A. Travlou<sup>1</sup>, Kavindra Singh<sup>1</sup>, Enrique Rodríguez-Castellón<sup>2</sup> and Teresa J. Bandoz<sup>1\*</sup>

Received 00th January 20xx,  
Accepted 00th January 20xx

DOI: 10.1039/x0xx00000x

www.rsc.org/

### Abstract:

Ammonia sensing capability of previously developed hybrid materials consisting of Cu-based MOF and either graphite oxide or aminated graphite oxide was investigated for the first time. The chips were exposed to continuous cycles of three different ammonia concentrations, followed by purging with dry air. The change in a normalized resistance was measured. All chips showed an irreversible increase in the resistance when initially exposed to ammonia indicating the chemical reaction of the target with their components. This resulted in the collapse of the MOF component. After signal stabilization/equilibration the chips were further tested for ammonia sensing and a reversible increase in the resistance was observed for all samples. Even though the crystalline porous structure of the sensing materials was no longer present, the ability of the resulting amorphous phase to weakly adsorb ammonia enabled the recording of electrical signal changes. The specific structure of the hybrid materials combined with the proximity of the Graphene phase, resulted in carrier mobility. A hybrid material with the smallest content of graphene phase exhibited the largest signal change upon exposure to ammonia. This was linked to the more developed MOF units in the case of this material, and therefore the larger involvement of the amorphous phase released by the collapse of MOF in the sensing mechanism. A linear relationship between the response of the sensors and the ammonia concentration was found. Combining the adsorption capacity of the hybrid materials with an electrical signal allows their application as components of safety devices.

### Introduction

Ammonia (NH<sub>3</sub>) is a colorless, pungent, and corrosive gas with high toxicity. It is a by-product of the manufacturing industry, fossil fuel combustion, and metabolic processes,<sup>1,2</sup> with an 55 ppm olfactory limit of detection.<sup>3</sup> Exposure to ammonia at low concentrations such as 50–100 ppm, can give rise to respiratory tract irritation while at even higher concentrations it may lead to fatal ailments. Therefore, its detection at low concentrations is necessary for environmental monitoring and chemical control in medical, industrial and agricultural fields.<sup>4,5</sup> Additionally, its detection may contribute to the detection of ammonium nitrate based explosives, since a trace of ammonia is released during the gradual decomposition of NH<sub>4</sub>NO<sub>3</sub>.<sup>6</sup>

The problems associated with the release of ammonia led to a growing interest and rapid progress in the field of ammonia gas sensors. Many studies have used carbon-based materials as

chemiresistive ammonia sensors, exploiting their ability to operate at room temperature, their conductive properties and the relative easiness of a device fabrication. Carbon nanotubes, micromechanical exfoliated graphene sheets, graphitic nano-ribbon films and reduced graphene oxide (rGO)/graphite oxide are examples of materials that have been shown as promising NH<sub>3</sub> sensors.<sup>5,7–14</sup> At ambient conditions these materials exhibit a p-type behavior where holes play the predominant role for a charge transfer. Therefore, when exposed to reducing gases, such as ammonia, hole depletion causes an increase in the materials' resistivity.<sup>7–11,15,16</sup> Despite their sensitivity, these carbon based material need to be functionalized (e.g. through metal doping) to improve their selectivity towards reducing gases.<sup>17,18</sup> Another group of carbonaceous materials investigated as ammonia sensors are nanoporous carbons. Recently we have shown that they not only able to detect ammonia but also can work as efficient protection media.<sup>19,20</sup> Another type of material, which has recently attracted the attention of scientists are porous crystalline solids, called metal-organic frameworks (MOFs). This class of solids is a 3D network of self-assembled metallic ions and polyatomic organic bridging ligands. Due to their very high porosity, and the diversity of both the metallic centers and organic ligands, they are used in variety of applications such gas storage, gas separation, and gas purification.<sup>21–29</sup>

In previous studies, it has been reported that composites that combine MOFs and graphene-based components, such as

<sup>1</sup> Department of Chemistry, The City College of New York  
160 Convent Ave, New York, NY, 10031, USA.

E-mail: tbandosz@ccny.cuny.edu; Fax: +1 212 650 6107; Tel: +1 212 650 6017

<sup>2</sup> Departamento de Química Inorgánica, Facultad de Ciencias, Universidad de Málaga, 29071 Málaga, Spain

\*Corresponding author: E-mail: tbandosz@ccny.cuny.edu; Fax: +1 212 650 6107; Tel: +1 212 650 6017

† Footnotes relating to the title and/or authors should appear here.

Electronic Supplementary Information (ESI) available: [details of any supplementary information available should be included here]. See DOI: 10.1039/x0xx00000x

DOI: 10.1039/x0xx00000x

graphite oxide and graphite oxide-urea composites, show an enhanced adsorptive performance towards the removal of small hazardous molecules such as  $\text{NH}_3$ ,  $\text{H}_2\text{S}$ ,  $\text{NO}_2$  or  $\text{H}_2$ .<sup>28,30-33</sup> The synergistic effect on porosity and chemistry leads to these significant improvements.<sup>28,34,35</sup> Composites of MOFs and aminated graphite oxide have been reported as excellent adsorbents of  $\text{CO}_2$ , which unlike ammonia, is an electron withdrawing gas.<sup>36,37</sup> Incorporation of aminated GO to MOF is considered advantageous not only because of the formation of new pores that enhance physical adsorption forces but also because it can lead to the improvement of adsorption selectivity based on specific interactions between the amino groups and acidic gases.<sup>38</sup>

Taking into account the good performance of MOF/GO composites as ammonia adsorbents,<sup>27</sup> here we examine the sensing response of this group of materials as a function of various ammonia concentrations. The MOF examined (HKUST-1) consists of  $\text{Cu}^{2+}$  dimer metal centers and benzene tricarboxylic (BTC) organic ligands with a chemical formula of  $\text{Cu}_3(\text{BTC})_2$ .<sup>39</sup> Even though these materials have been previously investigated in details,<sup>28,30,32,34</sup> the novelty of the approach used in this paper is in evaluation of their applicability as toxic gas sensors. HKUST-1 is a poor conductor of electricity because of the insulating character of the organic ligands and the poor overlap between the *p* and *d* orbitals of the  $\text{Cu}^{2+}$  ions.<sup>40</sup> Graphite oxide is also generally considered a poor conductor of electricity compared to graphite, or carbon black.<sup>41,42</sup> However, with GO-coated microchips having a resistance of  $37\ \Omega$  (according to our measurements), it has the potential to provide a measurable electrical signal during the sensing procedure. As discussed in the literature,<sup>33,34,43</sup> the incorporation of GO to the hybrid materials with MOF favors dispersive forces while maintaining the specific interactions between ammonia and the MOF metallic sites as well as with the functional groups of the organic linkers. Moreover, the addition of GO and its chemical bonds with MOF is expected to increase the materials' conductivity, which is of paramount importance for chemiresistive gas sensing.<sup>40,44,45</sup> Hence, we reasoned that the synergistic effect on porosity, chemistry and conductivity between the two components of the hybrid materials is capable of creating a mechanism for charge carrier mobility.

So far the concept of using porous adsorbents as sensors has been addressed for such materials as nanoporous carbons in our previous works.<sup>19,20</sup> Using MOF/GO composites as sensing materials broadens this concept towards another category of materials with high adsorption capacities for toxic gases. Therefore, the objective of this paper is to examine for the first time the sensing response of Cu-based MOF/graphene hybrid materials to ammonia gas at low concentrations, and to demonstrate how the surface chemistry and porous structure of them affects the electrical response of the sensor. The surface chemistry and textural features such as porosity and surface area were analyzed before and after ammonia adsorption, and considered in the context of the sensing behavior. The novelty of this study is in the application of MOF-graphene based hybrid materials for the first time as ammonia sensors with protective properties against the toxic gas. More

precisely, combining the high adsorption capacity of these materials with an electrical response, allows their application as components of safety devices, which by adsorbing ammonia and simultaneously measuring the air quality, limit the users' exposure.

## Results and discussion

Fig.1 shows the normalized resistance ( $R_t/R_0^{-1}$ ) of the MOF-GO and MOF-GOU hybrid material covered chips and how it changes when initially exposed to 500 ppm of ammonia. The hybrid materials are referred as MG25, MGU25, MG50 and MGU50 where M refers to MOF, G and GU- to Graphite oxide and aminated, GO respectively and 25 and 50 represent the weight percentage of the graphene -based phase in the hybrid materials. For MOF, no electrical signal change was detected due to its poor conductivity as aforementioned and therefore the results obtained on this material are not discussed in this paper.<sup>40</sup> Graphite oxide, on the other hand, is generally considered a poor conductor of electricity (compared to other carbons).<sup>41,42</sup> However, with microchips having a resistance of  $37\ \Omega$ , it provided a measurable electrical signal that increases when exposed to 500 ppm of ammonia, as seen in Fig. 1C. For all four samples, exposure to ammonia increases the resistance, and the extent of that increase is greater for those samples with lower content of GOs (Fig. 1A).

During this initial exposure it is likely that chemical reaction of ammonia with the MOF components took place.<sup>34,43</sup> Here, it formed complexes with the copper sites of HKUST-1, subsequently releasing the BTC ligands that in turn reacted with ammonia.<sup>33,34,46,47</sup> The collapsed MOF components that likely remain after ammonia exposure, will be referred to as the amorphous phase. Simultaneously, ammonia may also react with the oxygen functional groups of GO.<sup>29</sup> According to Bekyarova and co-workers,<sup>48</sup> when ammonia reacts with an organic chain that is bound to a conductive phase (such as carbon nanotubes or modified graphene phase, as in our case) there is a subsequent change in the electric property of the conductive phase that is equivalent to an increase in the electron donating sites on its surface. In the case of our hybrid materials, where GO and GOU are p-type conducting phases,<sup>16,49</sup> electron donation (to GO and GOU phases) through the organic linker (BTC), would result in a decrease in their conductivity, due to the depletion of the charge carriers (holes). Such an effect may be responsible for the increase in resistance seen in Fig. 1A, upon the exposure to ammonia. A similar signal would be also generated through the direct reaction of ammonia with the graphene phase.<sup>33</sup> Based on the data collected in Fig. 1A, MG25 and MGU25 exhibit a greater signal change compared to MG50 and MGU50 upon exposure to ammonia.

In order to examine the existence of synergistic effects, a few baseline experiments were done by testing ammonia sensing on microchips coated with CuO, Cu-BTC, GO and GOU. While the CuO chip didn't give any electrical signal, the resistivity of Cu-BTC was also too high to get any measurable signal change. When microchips were coated with GO and GOU

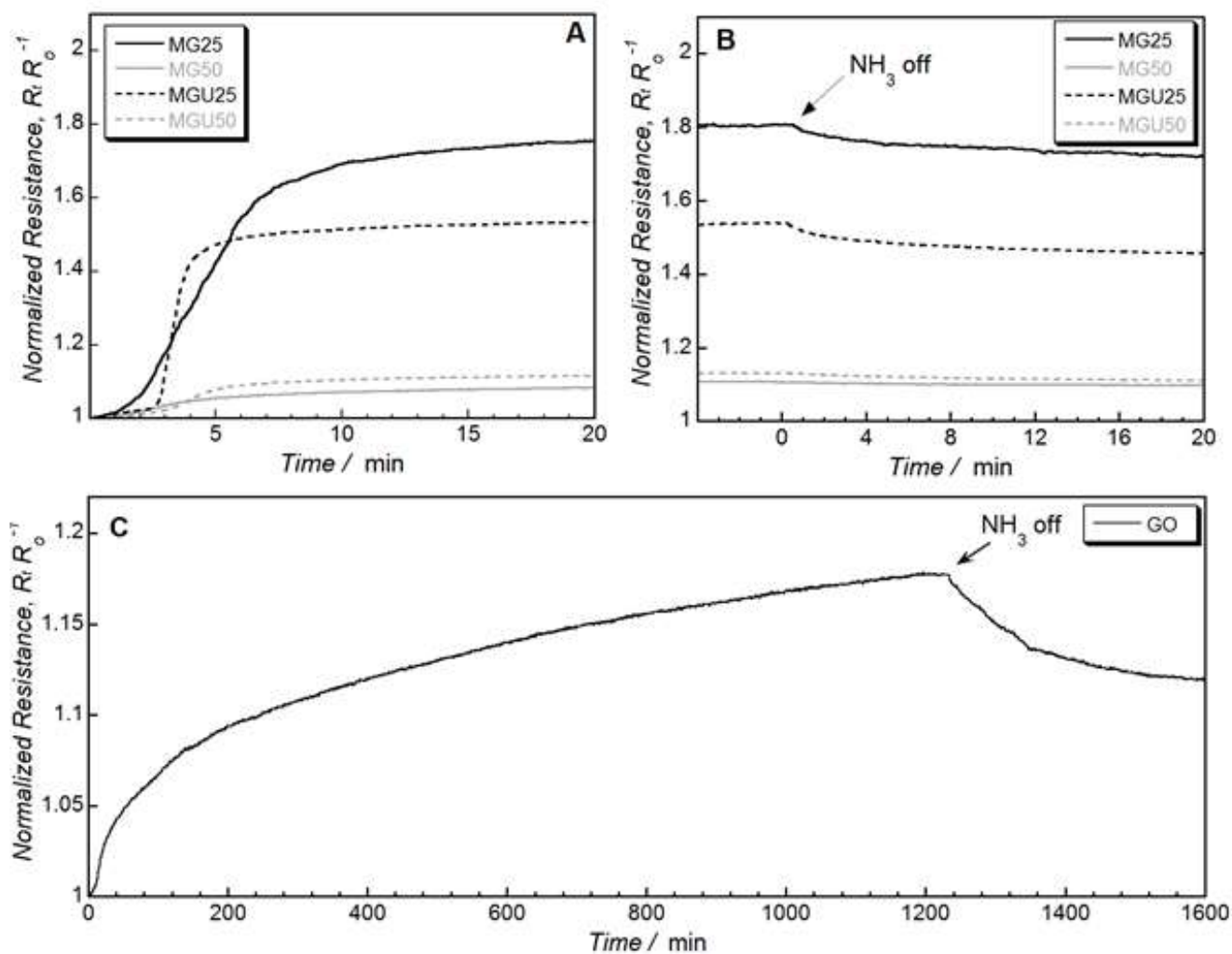


Fig. 1. Normalized change in resistance of the MOF/GO and MOF/GOU hybrid materials upon initial exposure to 500 ppm of ammonia (A) and subsequent purging with air after stabilization (B), and normalized change in resistance of GO upon initial exposure to ammonia and subsequent purging with air (C).

they got destroyed, likely due to the high acidity of GO and therefore the obtained results were inconsistent, with the normalized resistance varying between 0.3% - 1.2% over time. The microchips were initially exposed to 500 ppm of ammonia until the signal stabilized. That stabilization should be equivalent to the exhaustion of the reactive sites of the hybrid materials. At this point, ammonia was turned off and the sensor was purged with dry air until the system reached plateau in the electrical response. As seen from Fig. 1B, the signal for all samples decreases by a relatively small amount upon purging with air. This indicates that most of the reactions between ammonia and the hybrid materials are irreversible.

After the initial exposure and the stabilization of the signal (irreversible adsorption), the sensors were further tested to explore the extent of reversible sensing, if any. For this purpose the chips were exposed to different ammonia concentrations, varying from 100 to 500 ppm. The results are presented in Fig. 2 and Table 1. The samples whose surface features were stabilized by the initial exposures to ammonia are referred to with the suffix S added to their names. The reversible signals

were measured. Such a behavior is one of the requirements for effective sensing devices.

The extent of the change in the normalized resistance of the equilibrated sensors upon exposure to air depends on the ammonia concentrations (Fig. 2 and Table 1). Even though these changes cannot be considered as large, they are consistent and it is clearly seen that the chips tested exhibit reversible sensing. When these chips are purged with air, ammonia is apparently removed. Those sites that took part in the reversible adsorption during the initial exposure, become now available to interact

Table 1. Change of normalized resistance ( $R_t/R_0^{-1}$ ) of the MG and MGU hybrid materials upon exposure to different ammonia concentrations

NH <sub>3</sub> (ppm)	% change of normalized resistance ( $R_t/R_0^{-1}$ )			
	MG25-S	MG50-S	MGU25-S	MGU50-S
100	4	0.6	1.7	0.6
250	5.7	1.0	2.8	0.9
500	7	1.4	3.7	1.2

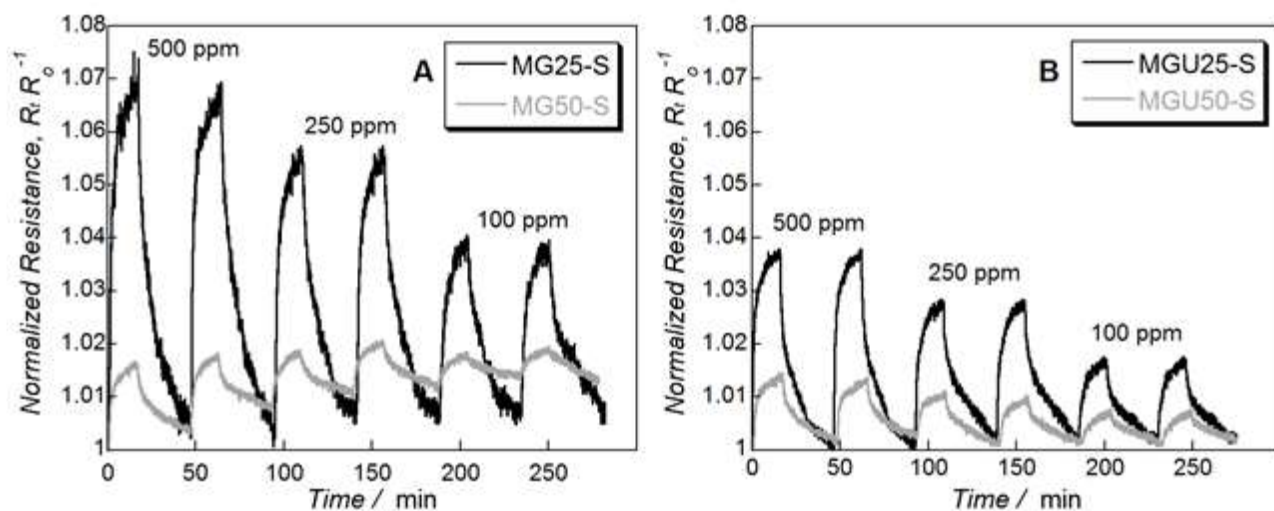


Fig. 2. Typical response curves for MOF/GO (A) and MOF/GOU (B) hybrid materials exposed to various ammonia concentrations, after the initial stabilization.

with ammonia, consequently changing the electrical property of the hybrid materials.

To show the reproducibility of the results, error bars representing the standard deviations from the mean based on exposure to 500 ppm of  $\text{NH}_3$  of three different microchips made of each sample are presented in Fig. 3. The relative standard deviation (%RSD) was found to be between 5.3-9.8 %.

Although similar MOF-GO composites have previously been studied as  $\text{NH}_3$  adsorbents,<sup>34,43,50</sup> the extensive characterization of the new batch used in this study will be presented here to derive the sensing mechanism and to account for differences in the materials' performance.

The ammonia breakthrough curves for the hybrid materials tested at dry ambient conditions, and the corresponding adsorption capacities are presented in Fig. 4. MOF exhibits the longest breakthrough time, but based on the shape of its desorption curve, its interaction with ammonia is the weakest compared to other materials tested. The steep breakthrough and desorption curves imply fast kinetics of interaction between the surface and ammonia and a relatively strong retention of

the latter on the surface. Of the samples tested, the desorption curves of the hybrid materials are much steeper than that of MOF itself; this is especially the case for MGU50.

The ammonia adsorption capacities of MOF-GO and MOF-GOU hybrid materials decrease with an increase in the carbon phase content. This is in agreement with the findings of a previous study by Petit and Bandoz,<sup>43</sup> that showed that the addition of GO to MOF improves the adsorption capacity, up to 18 wt. % GO in the composite. In the same study it was shown that when the GO content is high, similar to that used in this work, the structure of MOF gets distorted due to the limited formation of MOF units in the composites. This observation, explains the decreased capacity values of our hybrid materials with a graphene content of 50%.

The parameters of porous structure of the hybrid materials before and after exposure to ammonia are summarized in Table 2. Letter E represents samples exposed to ammonia in the breakthrough test. As seen from the table, MOF has the largest surface area ( $1267 \text{ m}^2 \text{ g}^{-1}$ ) compared to the hybrid materials, and it has a significant volume of micropores. This agrees with its higher adsorption capacity compared to the MG and MGU, as discussed earlier. A closer look at the parameters of porous structure and the breakthrough capacity values shows that there is a linear trend between the measured surface area and ammonia uptake. It is also notable that the volume of micropores decreases as the GO and the GOU contents increase, for both sets of hybrid materials. This trend shows that

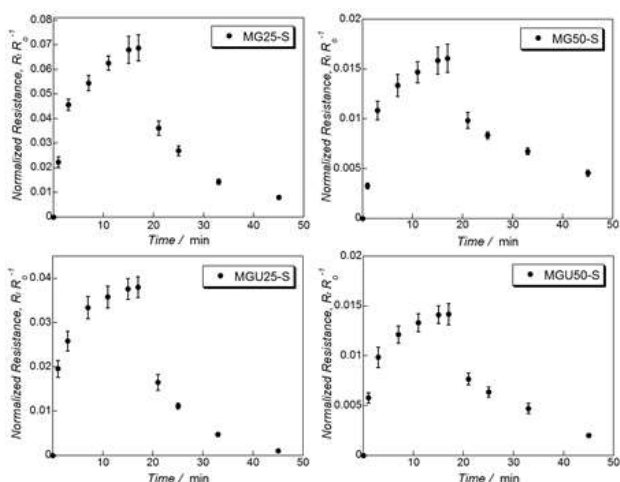


Fig. 3. Error bars representing the standard deviation from the mean for ammonia sensing at 500 ppm for MG25-S, MG50-S, MGU25-S and MGU50-S hybrid materials.

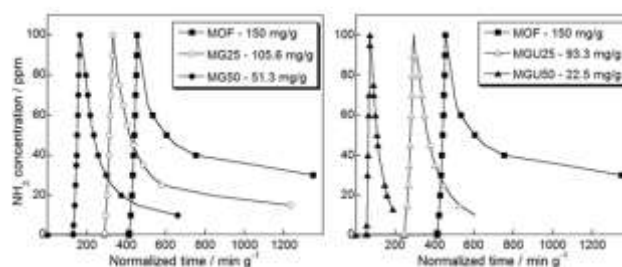


Fig. 4. Ammonia breakthrough and desorption curves for MOF and the hybrid materials along with the calculated breakthrough capacity.

**Table 2.** Parameters of Pore Structure Calculated from Adsorption of Nitrogen. Letter E represents samples exposed to ammonia in the breakthrough test.

Sample	$S_{\text{BET}}$ ( $\text{cm}^2 \text{g}^{-1}$ )	$V_{\text{micro}}$ ( $\text{cm}^3 \text{g}^{-1}$ )	$V_{\text{meso}}$ ( $\text{cm}^3 \text{g}^{-1}$ )	$V_{\text{t}}$ ( $\text{cm}^3 \text{g}^{-1}$ )	$V_{\text{micro}}/V_{\text{T}}$
MG25	916	0.391	0.103	0.494	0.79
MG50	434	0.173	0.114	0.287	0.60
MG25-E	83	0.012	0.088	0.100	0.12
MG50-E	91	0.024	0.085	0.109	0.22
MGU25	733	0.302	0.114	0.416	0.73
MGU50	399	0.150	0.135	0.285	0.53
MGU25-E	53	-	0.095	0.099	-
MGU50-E	64	-	0.123	0.125	-
MOF	1267	0.515	0.169	0.684	0.75
MOF-E	29	0.004	0.036	0.040	0.10
GO	9.2	-	0.014	0.014	-

the MOF is the primary contributor to the micro porous structure of these materials.

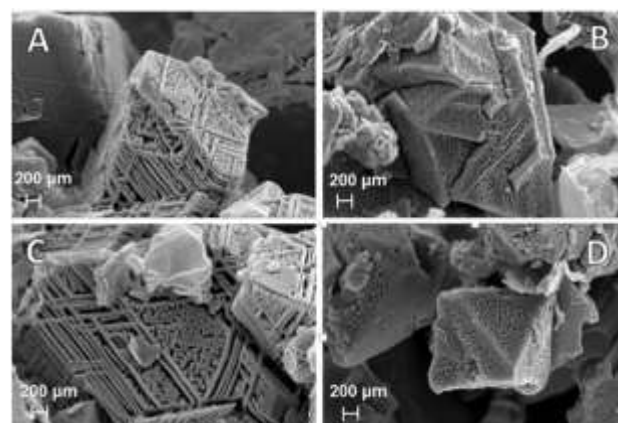
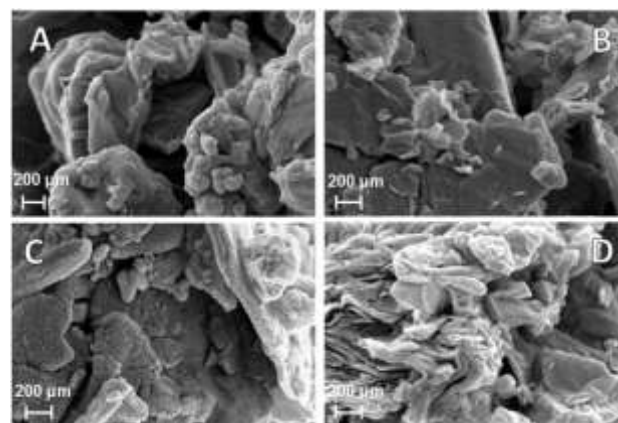
After ammonia adsorption the surface areas of MG25 and MG50 decreased significantly (91% and 79% respectively) but some porosity still exists, mainly in the range of mesopores. The decrease in surface area results from the collapse of the MOF units, as the strong interactions of ammonia with the copper centers break the Cu-O linkages. Interestingly, while a small volume of micropores is still detected for MGO hybrid materials, the microporosity of the MGUs is almost totally lost after exposure to the gas. Nevertheless, both exposed samples still exhibit relatively high volume of mesopores. These mesopores likely exist within the GO-formed scaffold.<sup>29</sup>

In a previous study by Petit and Bandoz,<sup>51</sup> the mechanism of the formation of the composites was examined and analyzed. It was found that the copper sites of HKUST-1 can react with the epoxy, hydroxylic, sulfonic and carboxylic functionalities of GO. These interactions were verified through the thermal analyses. Since the copper complexes have an octahedral geometry, the oxygen functional groups of the graphene phase can act either as equatorial (replacing a BTC molecule) or axial ligands (replacing a molecule of water). Some examples of the possible ways of coordination between the HKUST-1 and different functional groups of GO are presented in Fig. S4 of Supplementary Information. It is important to note that the current study is carried out in the absence of water.

SEM images provide details about the morphology of our materials. The materials with a 25% graphene phase (MG25 and MGU25) consists of MOF crystals embedded between exfoliated GO layers (Fig. 5A and 5C), while for those materials with 50 % GOs (MG50 and MGU50) the MOF's crystallinity is lacking. As seen from Fig. 6A, MG50 has very small particles of MOF deposited on the agglomerates of GO flakes, while for MGU50 (Fig. 6C) some irregular particles are visible on crystals and the GOU phase seems separated from the MOF. For MG25 and MGU25 after ammonia adsorption, the structure consisting of MOF crystals with embedded GO layers is destroyed owing to the reactive adsorption and thus to the collapse of MOF units.

This leaves amorphous MOF components embedded between the GO scaffold (Fig. 5B and 5D). The changes in the texture are also illustrated in Fig. 8. On the other hand, for MG50 and MGU50, the distorted graphene-based layers seem to remain as agglomerates (Fig. 6B and 6D).

The HRTEM micrographs are presented in Fig. 7. In the case of MG25 and MGU25 the lattice structure of the hybrid

**Fig. 5.** SEM images of MG25 (A), MG25-E (B) and MGU25 (C), MGU25-E (D) hybrid materials.**Fig. 6.** SEM images of MG50 (A), MG50-E (B) and MGU50 (C), MGU50-E (D) hybrid materials.

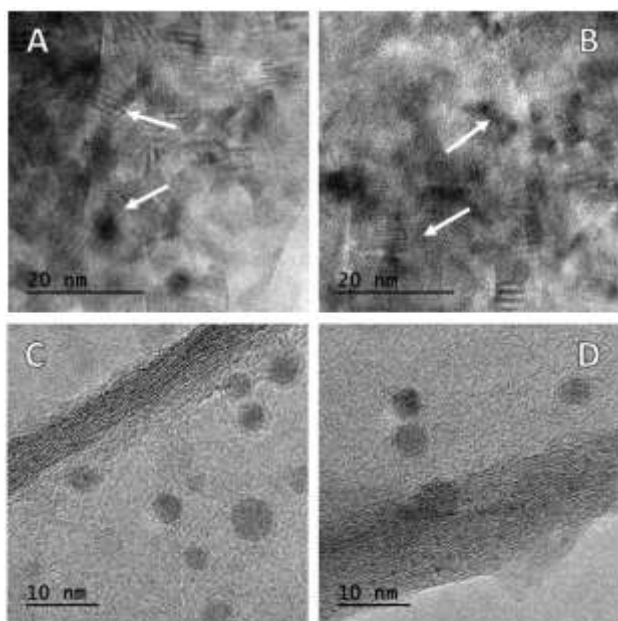


Fig. 7. HRTEM images of MG25 (A), MGU25 (B), MG50 (C) and MGU50 (D) hybrid materials.

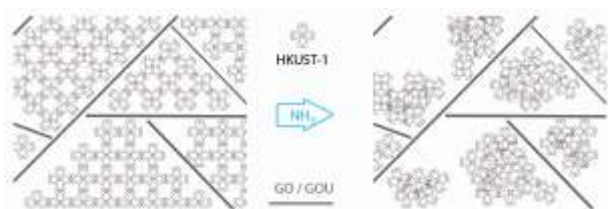


Fig. 8. Crystal structure of HKUST-1 and changes in the texture of the hybrid materials upon exposure to  $\text{NH}_3$ .

materials resulting from the MOF crystals embedded between exfoliated GO layers is clearly seen. On the other hand, in the case of MG50 and MGU50, even though small MOF particles can be observed, the GO distorted graphene-based sheets are predominant. These differences in the texture and the lack of contact between the MOF units in the case of MG50 and MGU50 might be responsible for the smaller signal change measured on the chips coated with these materials.

The FT-IR spectra of the parent materials, as well as the hybrid materials before and after exposure to ammonia are presented in Fig. S1 of Supplementary Information. The four hybrid materials seem to exhibit features similar to the initial MOF.<sup>43</sup> However, the changes in the environment of the carboxylate ligands, which are likely related to the distortion of the MOF structure caused by the incorporation of GO and thus the interactions of the ligands with the graphene phase, are seen from the variations in the ratios of the bands between  $1370 - 1643 \text{ cm}^{-1}$ . The appearance of a new peak at  $\sim 1643 \text{ cm}^{-1}$  for the hybrid materials could be also attributed to the presence of GO and GOU.

X-ray diffraction patterns of the parent materials and the hybrid materials before and after exposure to ammonia are presented in Fig. S2 of Supplementary Information. It was shown that after ammonia adsorption the intensity of the

characteristic peaks attributed to MOF significantly decreases, especially for the materials with the lowest graphene content (whose crystallographic structure is almost totally lost). For those materials with 50 % of graphene phase, some crystallinity still remains after exposure to ammonia. This might be related to the short breakthrough times since the material's limited porosity would hinder ammonia's access to the micropores.

The DTG curves obtained from the thermal analyses of our materials are presented in Fig. S3 of Supplementary Information. Once again, the hybrid materials and their exhausted counterparts exhibit DTG curves similar to the initial MOF. For the exhausted samples however, the peak that is attributed to the collapse of the MOF structure and the consequent release of  $\text{CO}_2$ ,<sup>51,52</sup> is shifted to a lower temperature. This shift in temperature is due to the weaker bonding between copper centers and BTC ligands upon ammonia complexation.

Table 3. Content of elements on the surface (in at % from XPS analysis)

Sample	XPS (at %)			
	C	O	N	Cu
MG25	67.4	23.1	4.6	4.9
MG25-E	68.8	22.3	5.6	3.3
MGU25	71.9	18.5	6.2	3.4
MGU25-E	73.0	18.6	5.7	2.9

XPS analysis was carried out in order to better understand the nature of the functional groups present on the surfaces of the hybrid materials. The content of elements in atomic percentage (at %) and the results of the deconvolution of the C 1s, O 1s and N 1s and Cu  $2p_{3/2}$  are given in Tables 3 and 4, respectively. Letter E represents samples exposed to ammonia in the breakthrough test.

The presence of nitrogen in the initial samples is linked to the small amount of DMF. As indicated above the samples were activated at  $120 \text{ }^\circ\text{C}$ . An increase in the nitrogen content for MGU25 in comparison with that in MG25 is related to the presence of urea. From the deconvolution of O 1s core energy levels it is seen that the relative concentration of oxygen in Cu-O group increased for the urea-modified sample. This is probably related to the reaction of urea with the epoxy groups of GO, which form complexes with the Cu centers of the HKUST-1 units (Figure S4b of Supplementary Information). The reaction would lead to the opening of the epoxide ring and the formation of Cu-O and  $-\text{NH}_2$  groups. The formation of the latter species in the case of the urea-treated sample is further verified from the deconvolution of N 1s core energy levels, where the relative concentration of nitrogen in amine groups increases. The increased relative concentration of oxygen in Cu-O in the case of the MGU25 sample can be also explained by the reaction of urea with the carboxylic acids of GO (Figure S4a of Supplementary Information). This is in agreement with the decreased relative concentration of oxygen in carboxylic acids for the urea-treated sample, as seen from the deconvolution of O 1s core energy levels.

**Table 4.** The results of deconvolution of C 1s, O 1s and N 1s core energy levels.

Binding energy, eV	Bond assignment	MG25	MG25-E	MGU25	MGU25-E
<b>C 1s</b>					
284.8	C-C (sp <sup>2</sup> carbon)	44.64	48.32	48.94	54.72
286.3	C-O, C-H (phenolic, alcoholic, etheric) or C-N, C-NH <sub>2</sub>	33.46	34.39	28.73	29.74
287.4	C=O (carbonyl or quinone) or C=N- (imine)	11.00	8.73	15.21	9.43
288.3	O-C=O (carboxyl or ester)	10.90	8.56	7.11	6.11
<b>O 1s</b>					
530.8	Cu-O	21.80	28.62	27.49	31.92
532.5	C=O in carboxylic acids	78.20	71.38	72.51	68.08
<b>N 1s</b>					
397.6	Aromatic nitrogen, Pyridine	10.13	11.58	11.70	14.34
399.7	C-NH <sub>2</sub> , NH amide, C=N- imine	30.00	37.12	34.08	42.31
401.5	, HCON(CH <sub>3</sub> ) <sub>2</sub> , Pyridine-N-oxide	59.86	51.29	54.22	43.35
<b>Cu 2p<sub>3/2</sub></b>					
932.7	Cu <sub>2</sub> O, Cu-O	32.49	35.20	34.68	39.76
934.9	Cu(OH) <sub>2</sub> , (COO) <sub>2</sub> Cu, Cu-epoxy	67.51	64.80	65.32	60.23

The comparison of the aminated and non-aminated hybrid materials shows that for MGU25 the relative concentration of carbon in C-O groups decreased and the relative concentration of N in amide groups increased. This is attributed to the chemical reaction of urea with the -OH groups of GO that form complexes with the copper centers, (Fig. S4C of Supplementary Information) leading to the formation of amides.

The deconvolution of O 1s core energy levels shows that after ammonia adsorption, the relative concentration of carbonyl groups in carboxylic acids decreased for the exhausted samples. This is in agreement with the proposed reaction of ammonia with the BTC units that are released after ammonia complexation to copper centers and the reaction of ammonia with the carboxylic groups of the graphene phase. Ammonia also reacts with carbonyl and epoxide groups of GO and GOU to form imine groups and aminoalcohols, respectively.<sup>53,54-56</sup> This is verified from the deconvolution of N 1s core energy levels, where the relative concentration of the imines or amines seems to increase for the exhausted samples. Ammonia reaction with carbonyl groups is further supported by the deconvolution of C 1s core energy levels for both GO and GOU, as the relative concentration of carbonyl groups decreases after ammonia adsorption. At the same time, its reaction with epoxide groups would lead to the epoxide ring opening and the formation of -NH<sub>2</sub> and -OH groups, which is verified from the increased relative concentration of oxygen in C-O groups, looking at the deconvolution of O 1s core energy levels, and the increased content of nitrogen in imine and amine groups, from the deconvolution of N 1s core energy levels.

It is important to mention that DMF was used as a solvent during the MOF synthesis and it was not totally removed by filtration/washing of the hybrid materials. This solvent (maybe with some impurities) must be seen in the deconvolution of N 1s core energy levels thus, the majority of nitrogen species with binding energy 401.5eV must represent nitrogen in DMF. The presence of Pyridine-N-oxide as an impurity cannot be

excluded. As seen from the deconvolution of N 1s core energy levels, exposure to ammonia, which a reducing gas led to a decrease in the contributions of pyridine-N-oxide species which is associated with an increase in the contribution of the pyridines in the exhausted samples.<sup>57</sup>

Based on the deconvolution of Cu 2p<sub>3/2</sub> core level spectra, it is seen that for the exhausted samples after exposure to ammonia, the relative contribution of copper in Cu(OH)<sub>2</sub>, (COO)<sub>2</sub>Cu, Cu-epoxy complexes decreased. We link it to the reaction of ammonia with the carboxyl groups of the coordinated to the copper centers BTC ligands, as well as with the carboxyl, hydroxyl and epoxy groups of graphite oxide (Fig. S4 of Supplementary Information), that are also coordinated to the copper sites in the initial samples. This would lead to the increased relative concentration of copper in the form of Cu<sub>2</sub>O, Cu-O for the exhausted samples as seen from the deconvolution of Cu 2p<sub>3/2</sub> core energy levels.

Based on the extensive surface characterization and the electrical response of the initial and exhausted samples, a sensing mechanism is derived. Interactions that can generate the irreversible sensing (as seen in Fig. 1) include ammonia complexation on the metal sites of MOF and interactions between the gas and the non-ordered amorphous phase. The latter include the acid-base interactions with the BTC ligands that are released after ammonia complexation to the copper centers, which lead to the formation of (NH<sub>4</sub>)<sub>3</sub>BTC. In that case, possible sources of the protons may be the acidic functional groups of GO and the uncoordinated BTC ligands. Finally direct interactions of the gas with the graphene phases also contribute to the generation of the irreversible signal.

The decreased porosity of MG50 and MGU50, compared to MG25 and MGU25, indicates less developed MOF units, seen as defects in the SEM images (Fig. 5 and Fig. 6). This limits the number of sites available for ammonia adsorption on the 50% GO phase samples, resulting in them having a less intense sensing signal (Fig. 1). Both series of samples reveal this trend.

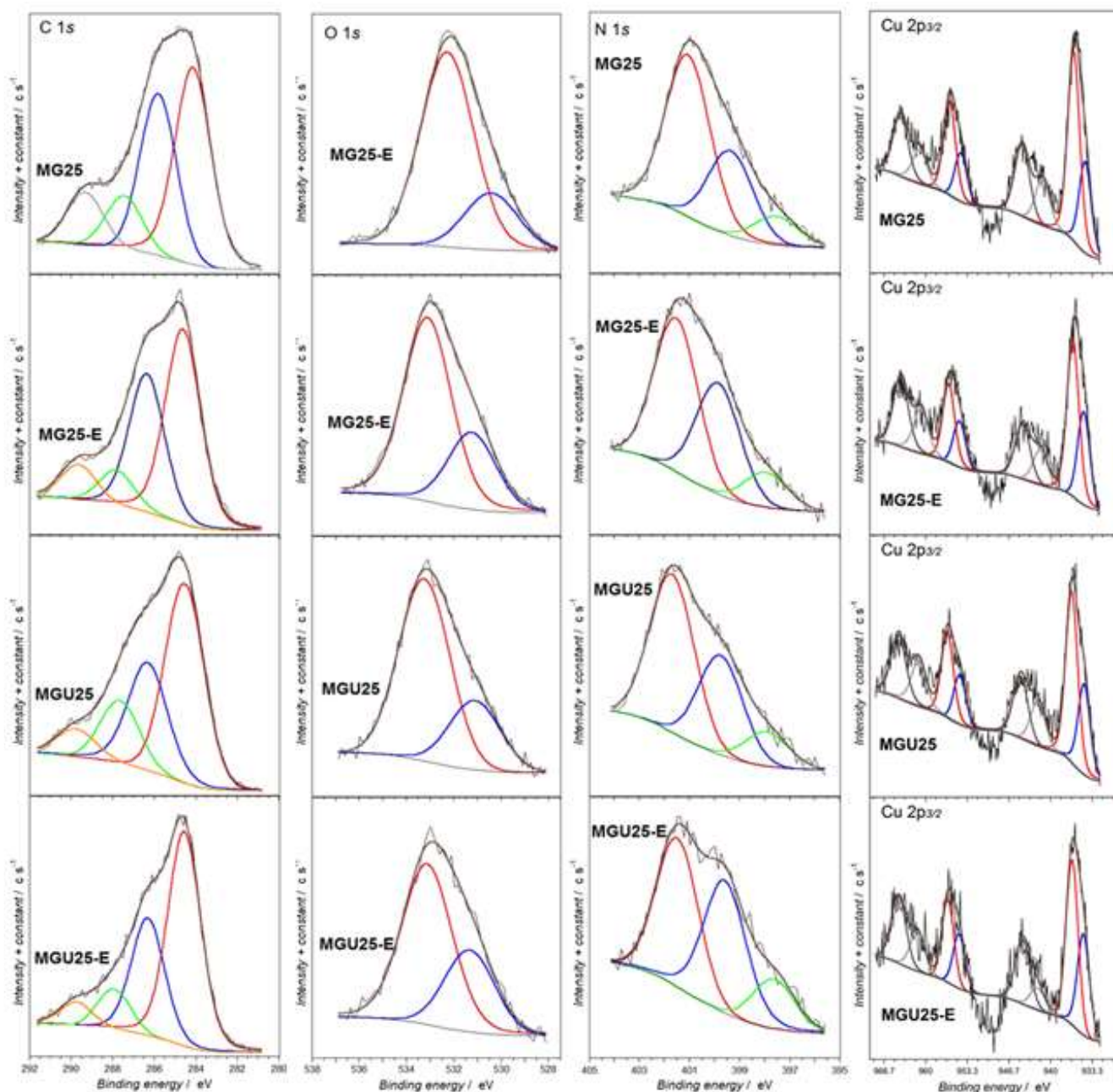


Fig. 9. C 1s, O 1s, N 1s and Cu 2p<sub>3/2</sub> core level spectra for MG25, MG25-E, MGU25 and MGU25-E.

Additionally, MG25 exhibits a greater increase in resistance, higher porosity and higher adsorption capacity compared to those of MGU25. However, it is notable that the latter reaches a stable signal faster than the former. More precisely, it takes only five minutes for MGU25 to reach equilibrium when exposed to ammonia, while MG25 requires 20 minutes (Fig. 1).

The reversible signal changes are attributed to physisorption in the altered pores and interactions with the graphene phases through dispersive forces such as hydrogen bonding with ammonia that is intercalated between the graphene layers.<sup>34</sup> Even though the porous structure of MOF should be mostly collapsed after the initial exposure to ammonia, the BTC acid should be present within the scaffold of the GO. Since the

ammonia's interactions with the BTC are weak/unstable it is easily desorbed when the system is purged with dry air. At this point, the BTC will become available for further reaction. This process of adsorption/desorption of NH<sub>3</sub> on the BTC can also be a source of the reversible signal recorded. All of these interactions are related to a subsequent change in the electric property of the hybrid materials, that is equivalent to an increase in electron donating sites on the conductive phase that has p-type behavior (due to the polarized oxygen functional groups attached to its layers).<sup>49</sup>

The results collected in Fig. 2 and Table 1 show that MG25-S exhibits a two times greater signal than MGU25-S for all three ammonia concentrations, while the performance of MG50-S and MGU50-S is about the same. The greater signal changes for the samples with a smaller content of the graphene based phase support the hypothesis that the MOF components, or more precisely the amorphous phase consisting of the chemicals released by the collapse of MOF, are involved in the sensing mechanism. The presence of the graphene phase might be crucial for the transport of electric charge. At the same time, this phase has carboxylic groups that ammonia can also react with. The smaller signal generated by MGU25-S than MG25-S might be explained by MGU25-S's initial modification where carboxylic acid were replaced with amines. In the case of MG50-S and MGU50-S, the dense structure and stacking of the graphene sheets prevents the rapid penetration of ammonia molecules into the inner space, hereby limiting the complete interaction between ammonia, copper sites, BTC and GO sheets.<sup>15</sup> This leads to a lower electrical signal change that is similar for both hybrid materials. The conductivity of both GO and GOU should also play a role in the observed results. Indeed, the conductivity of GOU was found to be  $2.78 \times 10^{-9} \text{ Sm}^{-1}$ , which is smaller than that of GO ( $1.1 \times 10^{-8} \text{ Sm}^{-1}$ ).

Considering that the amorphous phase originating from the collapse of the MOF structure seems to play an important role in the reversible sensing, physical mixtures consisting of BTC/copper nitrate hemipentahydrate/GO (1:2:1 and 1:2:3) were prepared in order to test their sensing response upon exposure to ammonia. Interestingly, the resistivity of the physical mixtures was too high to provide measurable signal changes. Moreover, the coated chips got destroyed as in the case of pure GO coated chips, due to the high acidity of the latter material. The above findings indicate that even though in the composites amorphous inorganic phase is present after the first exposure to ammonia, the synergistic effect of both original components is still able to alter their electric properties. It is likely that the formation of bonds between the MOF and GO reduced the GO phase resulting in a decrease in its acidity.

FTIR analysis (Fig. S1) suggests that the bands between  $1370 - 1643 \text{ cm}^{-1}$  visible in the spectra of the hybrid materials are related to changes in the environment of the carboxylate ligands upon their interaction with the graphene phase. The same peaks, however of a smaller intensity, are still present in the spectra for the exhausted samples and especially those with the lowest content of GO. As a result of the chemical interactions of the GO phase with the MOF components electrical changes occurring upon exposure of the samples to ammonia are linked to an increase in electron donating sites on the former phase. The lack of the chemical bonds between GO and the amorphous phase that function as a "chain effect" is likely responsible for the non-measurable signal changes in the case of the physical mixtures. Considering that measurable adsorption of ammonia on collapsed MOF has been previously reported by Petit and co-workers,<sup>34</sup> the novelty of this work is in the simultaneous detection combined with a protection capability of the MOF/GO hybrid materials against ammonia.

Table 5. Comparative table of the sensing performance of different graphene-based materials for the detection of  $\text{NH}_3$ .

Graphene-based sensing materials	Name	$\text{NH}_3$ concentration (ppm)	Response of the sensor (%)	References
GF	Graphene foam	1000	30	[58]
Bare RGO & RGO-PANI	Reduced graphene oxide-polyaniline	50	5.2 & 59.2	[59]
PG	Reduced graphene oxide-polypyrrole	125	13.2	[60]
Graphene-PEDOT:PSS	graphene-poly(3,4-		9.6	
PEDOT:PSS	ethylenedioxythiophene):poly(styrenesulfonate)	500	4.4	[61]
Graphene	(PEDOT:PSS)		2.4	
Graphene-AuNPs	Graphene decorated with gold nanoparticles	58	8	[62]
AuNPs-rGO	(-COOH) functionalized gold NPs-reduced graphene oxide	60	2.5	[63]
Graphene-PtNPs	Graphene films decorated with platinum NPs	58	12	[64]
Bare GNF & GNF-Pt	Graphitic nanoribbon films-platinum NPs	50	16.5 & 70	[65]
RGO/3-CuPc	Reduced graphene oxide/copper phthalocyanine	3200	15.4	[66]
$\text{MnO}_2/\text{GN}$	Tin oxide/graphene	50	15.9	[67]

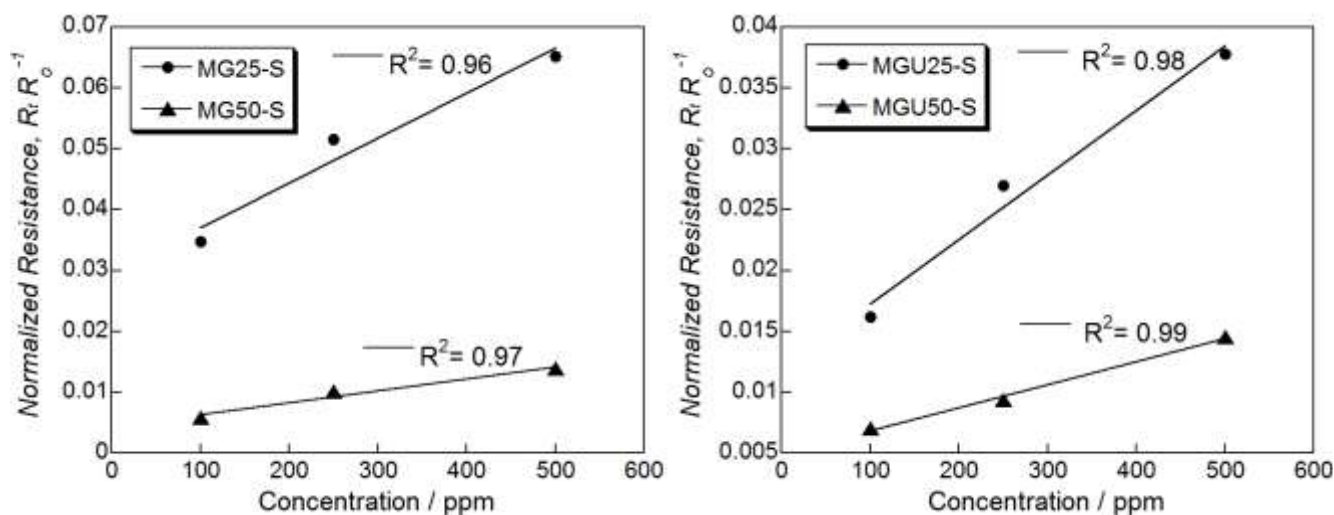


Fig. 10. The dependence of the change in normalized resistance of the MOF hybrid materials on the ammonia concentration in the challenge gas.

Since MOF/GO-based hybrids are investigated here as ammonia gas sensors, a table illustrating the sensing performance of other graphene-based materials is provided for comparison (Table 5). Taking into account that at this stage of our study the reversible sensing is mainly based on weak interactions of ammonia with the amorphous phase of the composite, the performance of our sensors can be considered as reasonable compared to other functionalized and non-functionalized sensors where a modified graphene phase is the main sensing element.

In a previous study where reduced graphene oxide was functionalized with polyaniline NPs, the sensor exhibited an improved sensitivity compared to the unfunctionalized RG.<sup>59</sup> More precisely, while bare RGO presented an about 5.2% signal change upon exposure to 50 ppm of ammonia, RGO-PANI hybrid showed a response of 59.2% at the same concentration. Johnson and coworkers studied the ammonia sensing properties of graphitic nanoribbon films (GNFs) functionalized with platinum nanoparticles.<sup>65</sup> They observed that the GNF-Pt sensor exhibited an about four times higher response at 50 ppm of  $\text{NH}_3$  (70%) compared to the unfunctionalized GNF (16.5%). In another study where graphene decorated with gold nanoparticles (AuNPs) was examined as ammonia gas sensor, it was found to exhibit an about 8% signal change at 58 ppm of the target gas.<sup>62</sup>

Table 5 indicates that in some other cases functionalization processes provided relatively low resistance changes or even smaller ones than those observed in our study. When a graphene:polymer-based composite (graphene-PEDOT:PSS) was exposed to 500 ppm of ammonia it exhibited a 9.6% change in the normalized resistance.<sup>61</sup> In another study where a reduced graphene oxide/copper phthalocyanine hybrid material was examined as an ammonia sensor a resistance change of only 15.4% was observed upon exposure to 3200 ppm of the target gas.<sup>66</sup> Finally, a sensor based on reduced graphene oxide functionalized with AuNPs was found to exhibit 2.5% signal change upon exposure to 60 ppm of  $\text{NH}_3$ .<sup>63</sup> Even though

the comparison of the different responses provided in Table 5 and the response of our best performing hybrid material (MG25-S) shows that MG25-S may not exhibit the best performance as an ammonia sensor, its response is comparable to many of the materials presented here. What we consider as of paramount importance concerning the performance of MG25-S (a material proven as an ammonia adsorbent) is that it is the first MOF-GO based hybrid material that has been shown to detect small toxic gas molecules through a chemiresistive method, while simultaneously protecting against them.

Fig. 10 shows that for all hybrid materials the change in the normalized resistance varies linearly with the concentration of ammonia; a desired feature of a gas sensor. The above observation indicates that the sensing mechanism does not change with increasing the gas concentration. Of the four samples tested, MG25 has the best performance since it has the greatest change in signal for each ammonia concentration.

## Conclusions

The results presented in this paper show that for the first time Cu-BTC MOF in combination with graphite oxide can be used as a low concentration gas sensor. The hybrid materials obtained by combining the crystalline order of MOFs with a graphene phase show improved electrical transport properties that enable their application as sensing materials. Even though the crystalline porous structure in the reversible sensors is no longer present, the ability of the amorphous phase (that is released by the collapse of MOF) to weakly adsorb ammonia within the proximity of the graphene based phase, enables the detection/recording of changes in the electrical signal. Adsorption at this point includes ammonia complexation to the metal sites, acid-base interactions with carboxylic groups of the ligands and direct interactions with the graphene phases that are responsible for the irreversible signal change, while physisorption in the unaltered pores, interactions with the graphene phases through dispersive forces and weak reaction

between ammonia and BTC acid, present at the GO scaffold, cause reversible sensing. The synergistic effect on conductivity between the two components of the hybrid materials is capable of creating a mechanism for carrier mobility. The electrical changes that are related to the above interactions are equivalent to an increase in electron donating sites on the conductive phase. Combining the adsorption capacity of MOF with an electrical conductivity of the graphene-based phase allows their application as components of safety devices, which by adsorbing ammonia and simultaneously measuring the air quality, limits the users' exposure. Of the materials tested, MG25 proved to perform the best.

Although this study has shown for the first time that Cu-BTC MOF/Graphene-based hybrid materials are capable of detecting ammonia (as sensors) while simultaneously adsorbing the gas at dry conditions, their sensing capability in moist conditions needs to be addressed and it is the topic of the ongoing research. Due to the complexity of the hybrid structure and the consequent changes in morphology during ammonia exposure, there was no specific characteristic(s) that could be the determinant of the overall performance of the materials as sensors. Further work needs to be done to fully distinguish which of the possible mechanisms identified in this paper are the primary contributor(s) to the sensing property of the MOF/Graphene-based hybrid materials.

## Experimental

### Materials

GO was prepared by oxidation of commercial graphite powder (Sigma Aldrich), using Hummers' method. The detailed preparation of GO is presented elsewhere.<sup>53</sup> The aminated GOU was prepared by dispersing of 1 g of GO in a 0.3 mol l<sup>-1</sup> aqueous solution of urea followed by stirring for 24 hours, filtration of the product and drying in air. A TA analysis indicated that about 2.5 % of urea was introduced to the surface of GO. For the preparation of the HKUST-1, copper nitrate hemipentahydrate (98%, Sigma Aldrich) was mixed with 1,3,5 benzenetricarboxylic acid (98%, Alfa Aesar) and the synthesis was done according to the procedure that is described by Millward and co-workers.<sup>68</sup> The solvents used during the synthesis were N,N dimethylformamide (DMF, 99.8%, ACS grade, BDH), ethanol (94-96%, ACS grade, BDH) and dichloromethane (99.5%, ACS grade, BDH). The preparation of the hybrid materials with the GO or GOU contents of 25 and 50%, respectively, of a final material was done following the method described by Petit and Bandoz.<sup>51</sup> Briefly the GOs were dispersed in the solution of the chemicals used to synthesize MOF and then all the steps used to synthesize MOF were followed. The hybrid materials are referred as MG25, MGU25, MG50 and MGU50 for 25% and 50% of the graphene composite, respectively. G and GU refer to graphite oxide and aminated graphite oxide, respectively.

### Preparation of sensor chips

For the preparation of the sensor, each composite was grounded and made into a slurry using DMF as solvent. The

slurry was then spread on to an 8 mm × 8 mm thin-film gold interdigitated electrode, with 50 μm lines/spaces on an alumina substrate, using a blade and finally dried at 150 °C for 24 hours.

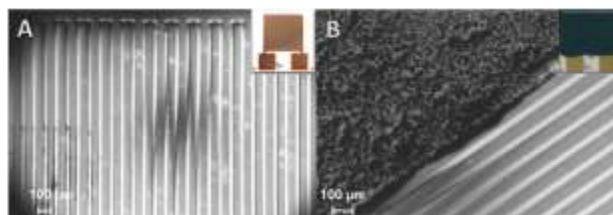


**Fig. 11.** Scanning electron micrographs and digital images of the chips before coating (A) and after coating (B) with the hybrid materials' slurry.

## Electrochemical measurements

### Sensing procedure

For the sensing tests, each microchip was placed in a 20 cm<sup>3</sup> gas chamber and purged with dry air to establish a dynamic equilibrium. This methodology has been applied previously to test the nanoporous carbon chips.<sup>19,20</sup> The Electrical measurements and sensing performance were monitored using a VersaSTAT MC (AMETEK, Princeton Applied Research) via four-wire sensing at room temperature, while a 1V voltage was applied. Microchips were initially purged with dry air until the electrical signal stabilized. Then they were exposed to 100, 250 and 500 ppm of ammonia, with a flow rate 500 ml/min for 17 minutes, which was found as the time needed for the signal to reach a steady state. Next they were again purged with air to remove physically adsorbed ammonia and determine the role of chemisorption (irreversible processes) and porosity on the sensing signal. Such treated chips were then tested for sensing via reversible processes, by exposing them to ammonia for sixteen minutes followed by purging with air for thirty minutes. From the data obtained, the normalized resistance ( $R_t R_0^{-1}$ ) of the chips was calculated, where  $R_0$  and  $R_t$  are the resistance of the sensor initially, and at any time,  $t$ , during exposure to ammonia respectively.

### Methods

**XPS.** The elements present in the materials studied as well as their chemical state were identified by X-ray photoelectron spectroscopy (XPS) analysis. A Physical Electronics spectrometer (PHI 5700) was used with MgK $\alpha$  X-ray radiation (1253.6 eV) as the excitation source. High resolution spectra were recorded at a take-off angle of 45° by using a concentric hemispherical analyzer operating in constant-pass-energy mode at 29.35 eV, with a 720 μm diameter analysis area. Cu 2p and C 1s core level spectra were registered first with a low irradiation time (7 min) to avoid as much as possible photoreduction of Cu<sup>2+</sup>.

**Sorption of nitrogen.** On the materials obtained, sorption of nitrogen at its boiling point was carried out using ASAP 2020 (Micromeritics). Before the experiments, the samples were outgassed at 120 °C to constant vacuum (10<sup>-4</sup> kPa). From the isotherms, the surface areas (BET method), total pore volumes,  $V_t$  (from the last point of isotherm at a relative pressure equal to 0.99), and the volumes of micropores ( $V_{mic}$ ) and mesopore

( $V_{mes}$ ) were calculated. The pore size distributions were calculated using the Barrett-Joyner-Halenda analysis (BJH). It has to be mentioned here that our samples were activated at 120 °C and therefore a smaller surface of the MOF units is expected compared to other surface values that are reported in the literature<sup>51,69-71</sup>. This was an arbitrary choice to avoid the decomposition of the GO component.

**NH<sub>3</sub> breakthrough dynamic test.** Ammonia adsorption capacity was measured at room temperature, in dynamic conditions, using a laboratory designed test.<sup>28</sup> The adsorbent's bed contained about 2 cm<sup>3</sup> of glass beads well mixed with the amount of adsorbent required to obtain a homogeneous bed (between 50 and 120 mg for HKUST-1 and the hybrid materials). The mixture was packed into a glass column. The beads were used to avoid the pressure drop and thus to favor the kinetics of the breakthrough tests. The total flow rate of the inlet stream was 225 mL/min with an ammonia concentration of 1000 ppm in dry air.

Ammonia breakthrough was monitored using an electrochemical sensor (Multi-Gas Monitor ITX system) and its flow was arbitrarily stopped at the breakthrough concentration of 100 ppm. The adsorption capacity of each adsorbent was calculated by integration of the area above the breakthrough curve taking into account the ammonia concentration in the inlet gas, the flow rate, the breakthrough time, and the mass of adsorbent used. Error in the adsorption capacity is estimated to be about 10–15%. The suffix -E is added to the name of the samples after exposure to ammonia in dry conditions.

**Thermal analysis.** Thermogravimetric (TG) curves and their derivative (DTG) were obtained for all samples using a TA Instrument analyzer. About 30 mg of the carbon sample (initial or exhausted) were heated from 30 °C to 1000 °C under a flow of nitrogen (100 mL/min). The heating rate was 10 °C/min.

**FT-IR Spectroscopy.** FTIR Fourier transform infrared (FTIR) spectroscopy was carried out using a Nicolet Magna-IR 830 spectrometer using the attenuated total reflectance method (ATR). The spectrum was collected 32 times and corrected for the background noise. The experiments were done on the powdered samples without the addition of KBr.

**XRD.** X-Ray diffraction (XRD) patterns of as-synthesized grounded adsorbents were recorded using powder diffraction procedures on a Phillips X'Pert X-ray diffractometer, using a Cu<sub>Kα</sub> radiation (operated at 40 kV and 40 mA). The diffraction patterns were collected from 5° to 60° at absolute scan.

**SEM.** Scanning electron microscopy (SEM) images were obtained with a Zeiss Supra 55 VP. The accelerating voltage was 5.00 kV. Scanning was performed in situ on a sample powder without coating.

**HRTEM.** High resolution transmission electron microscopy (HRTEM) was performed on a JEOL 2100F instrument with an accelerating voltage of 200 kV. The analyses were conducted on samples previously suspended in ethanol.

## Acknowledgements

This work was supported by the ARO (Army Research Office) grant W911NF-10-1-0030 and W911NF-13-1-0225, and NSF

collaborative SBET Grant No. 1133112, and project CTQ2012-37925-C03-03 (Spin) and FEDER funds. KS is grateful to Drs Vojislav Krstic and Maria Kolesnik-Gray for the valuable training and fruitful discussion during his internship at the Trinity College.

## References:

1. B. Timmer, W. Olthuis and A. van den Berg, *Sens. Actuators, B*, 2005, **107**, 666–677.
2. C. Plog, A. Knezevic, H. Leye, R. Moos, R. Mu, E. Irion and T. Braun, *Sens. Actuators, B*, 2002, **83**, 181–189.
3. M. Bendahan, P. Lauque, C. Lambert-Mauriat, H. Carchano and J. L. Seguin, *Sens. Actuators, B*, 2002, **84**, 6–11.
4. Y.-S. Lee, K.-D. Song, J.-S. Huh, W.-Y. Chung and D.-D. Lee, *Sens. Actuators, B*, 2005, **108**, 292–297.
5. T. Hibbard, K. Crowley, F. Kelly, F. Ward, J. Holian, A. Watson and A. J. Killard, *Anal. Chem.*, 2013, **85**, 12158–65.
6. S. Pandey, G. K. Goswami and K. K. Nanda, *Sci. Rep.* 2013, **3**, 2082.
7. P. Teerapanich, M. T. Z. Myint, C. M. Joseph, G. L. Hornyak and J. Dutta, *IEEE Trans. Nanotechnol.*, 2013, **12**, 255–262.
8. S. Yoo, X. Li, Y. Wu, W. Liu, X. Wang and W. Yi, *J. Nanomater.*, 2014, **2014**, 1–6.
9. S. Some, Y. Xu, Y. Kim, Y. Yoon, H. Qin, A. Kulkarni, T. Kim and H. Lee, *Sci. Rep.*, 2013, **3**, 1868.
10. A. Lipatov, A. Varezchnikov, P. Wilson, V. Sysoev, A. Kolmakov and A. Sinitskii, *Nanoscale*, 2013, **5**, 5426–34.
11. E. C. Mattson, K. Pande, M. Unger, S. Cui, G. Lu, M. Weinert, J. Chen, C. J. Hirschmugl, *J. Phys. Chem. C*, 2013, **117** (20), 10698–10707.
12. G. Chen, T. M. Paronyan, E. M. Pigios and A. R., *Sci. Rep.* 2012, **2**, 343.
13. J. L. Johnson, A. Behnam, Y. An, S. J. Pearton and A. Ural, *J. Appl. Phys.* 2011, **109**, 124301.
14. Y. Wang, L. Zhang, N. Hu, Y. Wang, Y. Zhang, Z. Zhou, Y. Liu, S. Shen and C. Peng, *Nanoscale Res. Lett.*, 2014, **9**, 251.
15. X. L. Huang, N. T. Hu, Y. Y. Wang and Y. F. Zhang, *Adv. Mater. Res.* 2013, **669**, 79–84.
16. H. K. Jeong, C. Yang, B. S. Kim and K. Kim, *Europhys. Lett.*, 2010, **92**, 37005.
17. A. Tilman, Ph.D. Thesis, Swiss Federal Institute of Technology Lausanne, 2007.
18. A. Abdelhalim, A. Abdellah, G. Scarp and P. Lugli, *Nanotechnology*, 2014, **25**, 055208.
19. K. Singh, N. A. Travlou, S. Bashkova, E. Rodríguez-Castellón and T. J. Bandoz, *Carbon*, 2014, **80**, 183–192.
20. N. A. Travlou, M. Seredych, E. Rodríguez-Castellón and T. J. Bandoz, *J. Mater. Chem. A*, 2015, **3**, 3821–3831.
21. R. J. Kuppler, D. J. Timmons, Q. R. Fang, J. R. Li, T. A. Makal, M. D. Young, D. Yuan, D. Zhao, W. Zhuang and H.-C. Zhou, *Coord. Chem. Rev.*, 2009, **253**, 3042–3066.
22. N. A. Khan, Z. Hasan and S. H. Jhung, *J. Hazard. Mater.*, 2013, **244-245**, 444–456.
23. K. Yang, Q. Sun, F. Xue and D. Lin, *J. Hazard. Mater.*, 2011, **195**, 124–131.

24. M. Eddaoudi, H. Li and O. M. Yaghi, *J. Am. Chem. Soc.*, 2000, **122**, 1391–1397.
25. P. Mishra, S. Edubilli, B. Mandal and S. Gumma, *J. Phys. Chem., C* 2014, **118**, 6847–6855.
26. D. Britt, D. Tranchemontagne and O. M. Yaghi, *Proc. Natl. Acad. Sci. U. S. A.*, 2008, **105**, 11623–11627.
27. J. B. Decoste and G. W. Peterson, *Chem. Rev.*, 2014, **114**, 5695–5727.
28. E. Barea, C. Montoro and J. R. Navarro, *Chem. Soc. Rev.*, 2014, **43**, 5419–5430.
29. J. R. Li, R. J. Kuppler and H. C. Zhou, *Chem. Soc. Rev.*, 2009, **38**, 1477–1504.
30. I. Ahmed and S. H. Jung, *Mater. Today*, 2014, **17**, 136–146.
31. C. Petit, B. Levasseur, B. Mendoza and T. J. Bandoz, *Microporous Mesoporous Mater.*, 2012, **154**, 107–112.
32. Z. Huang, G. Liu and F. Kang, *ACS Appl. Mater. Interfaces*, 2012, **4**, 4942–7.
33. T. J. Bandoz and C. Petit, *Adsorption*, 2010, **17**, 5–16.
34. C. Petit, L. Huang, J. Jagiello, J. Kevlin, K. E. Gubbins and T. J. Bandoz, *Langmuir*, 2011, **27**, 13043–13051.
35. G. Srinivas and Z. X. Guo, *Prog. Mater. Sci.*, 2014, **69**, 1–60.
36. Y. Zhao, H. Ding and Q. Zhong, *Appl. Surf. Sci.*, 2013, **284**, 138–144.
37. Y. Zhao, Y. Cao and Q. Zhong, *J. Clean Energy Technol.*, 2014, **2**, 34–37.
38. O. Shekhah, Y. Belmabkhout, Z. Chen, V. Guillermin, A. Cairns, K. Adil and M. Eddaoudi, *Nat. Commun.*, 2014, **5**, 4228.
39. S. S. Y. Chui, S. M. F. Lo, J. P. H. Charmant, A. Orpen and I. D., *Science*, 1999, **283**, 1148–1150.
40. A. Talin, A. Centrone, A. C. Ford, M. E. Foster, V. Stavila, P. Haney, R. A. Kinney, V. Szalai, F. El Gabaly, H. P. Yoon, F. Léonard and M. D. Allendorf, *Science*, 2014, **343**, 66–69.
41. S. Stankovich, D. Dikin and G. Dommett, *Nature*, 2006, **442**, 282–286.
42. D. R. Dreyer, S. Park, C. W. Bielawski and S. R. Ruoff, *Chem. Soc. Rev.*, 2010, **39**, 228–240.
43. C. Petit, B. Mendoza and T. J. Bandoz, *Langmuir*, 2010, **26**, 15302–15309.
44. M. Jahan, Q. Bao, J. Yang and K. P. Loh, *J. Am. Chem. Soc.*, 2010, **132**, 14487–14495.
45. M. D. Allendorf, A. Schwartzberg, V. Stavila and A. Talin, *Chemistry*, 2011, **17**, 11372–11388.
46. G. W. Peterson, G. W. Wagner, A. Balboa, J. Mahle, T. Sewell and C. J. Karwacki, *J. Phys. Chem. C*, 2009, **3**, 13906–13917.
47. T. Watanabe and D. S. Sholl, *J. Chem. Phys.*, 2010, **133**, 094509.
48. E. Bekyarova, I. Kalininkhaa, M. E. Itkis, L. Beer, N. Cabrera and R. C., *J. Am. Chem. Soc.*, 2007, **129**, 10700–10706.
49. G. Venugopal, K. Krishnamoorthy, R. Mohan and S.-J. Kim, *Mater. Chem. Phys.*, 2012, **132**, 29–33.
50. B. Levasseur, C. Petit and T. J. Bandoz, *ACS Appl. Mater. Interfaces*, 2010, **2**, 3606–3613.
51. C. Petit, J. Burrez and T. J. Bandoz, *Carbon*, 2011, **49**, 563–572.
52. Y. K. Seo, G. Hundal, I. T. Jang, Y. K. Hwang, C. H. Jun and J. S. Chang, *J. S., Micro. Mesopor. Mater.*, 2013, **119**, 331–337.
53. M. Seredych and T. J. Bandoz, *J. Phys. Chem.*, 2007, **111**, 15596–15604.
54. R. Yao, D. Zhao, L. Bai, N. Yao and L. Xu, *Nanoscale Res Lett.*, 2014, **9**, 368.
55. D. M. Roundhill, *Chem. Rev.*, 1992, **92**, 1–27.
56. R. W. Lyer, *Chem. Rev.*, 1963, **63**, 489–510.
57. D. Scott, M. J. Cooney and B. Y. Liaw, *J. Mater. Chem.*, 2008, **18**, 3216–3222.
58. F. Yavari, Z. Chen, A. V. Thomas, W. Ren, H.-M. Cheng, and N. Koratkar, *Sci. Rep.*, 2011, **1**, 166.
59. X. Huang, N. Hu, R. Gao, Y. Yu, Y. Wang, Z. Yang, E. Siu-Wai Kong, H. Wei and Y. Zhang, *J. Mater. Chem.*, 2012, **22**, 22488.
60. D. C. Tiwari, P. Atri, and R. Sharma, *Synth. Met.*, 2015, **203**, 228–234.
61. D. C. Tiwari, P. Atri, and R. Sharma, *Synth. Met.*, 2015, **203**, 228–234.
62. M. Gautam and A. H. Jayatissa, *Solid. State. Electron.*, 2012, **78**, 159–165.
63. X. Xia, S. Guo, W. Zhao, P. Xu, H. Yu, T. Xu, and X. Li, *Sens. Actuators, B*, 2014, **202**, 846–853.
64. M. Gautam and A. H. Jayatissa, *J. Appl. Phys.*, 2012, **111**, 094317.
65. J.L. Johnson, A. Behnam, Y. An, S. J. Pearton, and A. Ural, *J. Appl. Phys.*, 2011, **109**, 124301.
66. X. Zhou, X. Wang, B. Wang, Z. Chen, C. He, and Y. Wu, *Sens. Actuators, B*, 2014, **193**, 340–348.
67. Q. Lin, Y. Li, and M. Yang, *Sens. Actuators, B*, 2012, **173**, 139–147.
68. A. R. Millward and O. M. Yaghi, *J. Am. Chem. Soc.*, 2005, **127**, 17998–17999.
69. Y. Peng, V. Krungleviciute, I. Eryazici, J. T. Hupp, O. K. Farha, and T. Yildirim, *J. Am. Chem. Soc.*, 2013, **135**, 11887–11894.
70. T. Duren, F. Millange, G. Ferey, K. S. Walton and R. Q. Snurr, *J. Phys. Chem. C*, 2007, **111**, 15350–15356.
71. M. Klimakow, P. Klobes, K. Rademann and F. Emmerling, *Microporous Mesoporous Mater.*, 2012, **154**, 113.

